Acta Materialia 265 (2024) 119642

Contents lists available at ScienceDirect

Acta Materialia

journal homepage: www.elsevier.com/locate/actamat

Property and microstructure of $Ni_{50.3}Ti_{29.7}Hf_{20}$ high-temperature shape memory alloys with different aging conditions

Jiaqi Dong [a,1], Alexander Demblon [a,1], Tejas Umale [a], Dexin Zhao [a], Gianna Valentino [b], Ibrahim Karaman [a], Kelvin Y. Xie [a,*]

[a] Department of Materials Science and Engineering, Texas A&M University, College Station, TX 77843, USA
[b] Department of Materials Science and Engineering, University of Maryland, College Park, MD 20742, USA

ARTICLE INFO

Keywords:
Shape memory alloys
Martensite
Twinning
Transmission electron microscopy

ABSTRACT

NiTiHf is a class of promising high-temperature shape memory alloys (SMAs) that find many applications. However, their complex martensitic microstructure and attendant thermomechanical properties are not well understood. In this work, we used solution-treated (precipitate-free) and aged (precipitate-bearing) $Ni_{50.3}Ti_{29.7}Hf_{20}$ (at.%) SMAs as a model system. We observed that the presence of precipitates refines the martensite plates, reduces the number of martensite variants, and changes the orientation relationship between the martensite plates compared with the solution-treated counterpart. Furthermore, the aged samples exhibited higher transformation temperatures, narrower phase transformation temperature windows, improved thermal stability, and retained or even improved actuation strain. The improved thermomechanical properties observed in the aged samples are attributed in part to the reduction of the number of martensite variants and the change in martensite and twin interface characteristics, both of which are induced by the presence of precipitates. The findings of this study offer new information on the processing-property-microstructure relationship in NiTiHf-based SMAs. These insights can guide future materials design efforts, facilitating the development of advanced SMAs tailored for specific high-temperature applications.

1. Introduction

Shape memory alloys (SMAs) are a group of metallic materials that exhibit the unique ability to return to their original shape after deformation, making them valuable in various applications in aerospace, biomedical, automotive, robotics, consumer electronics, and energy system industries. Among SMAs, NiTi is widely used due to its exceptional shape memory property, superelasticity, corrosion resistance, and biocompatibility [1,2]. However, the limited transformation temperatures (<150 °C) of NiTi restricts its broader applications. To overcome this limitation, researchers have explored the addition of ternary elements to the NiTi system to elevate the transformation temperatures (TTs). Among these alloys (e.g., NiTiHf, NiTiPt, NiTiPd, NiTiAu, etc.), NiTiHf emerges as a promising choice with its relatively high transformation temperature, favorable shape memory properties, and relative cost-effectiveness [3–5]. Moreover, aging can induce second-phase precipitation in NiTi and NiTi-based SMAs, tailoring the matrix composition, martensite microstructure, and transformation behavior of these alloys [6–22]. The Ni-rich NiTiHf alloy contains precipitates known as H-phase, which was initially characterized by Han et al. in aged NiTiHf alloys. H-phase precipitates have been determined to have a face-centered orthorhombic crystal structure with a space group of *F 2/d 2/d 2/d* (No. 70) [23]. Yang et al. later proposed an atomic structural model for the precipitation process [6]. The precipitate structure has been identified as a superstructure of the B2 austenite phase [6,7,23]. The composition of H-phase precipitation is not specific, but is Ni-rich and Hf-rich compared to the matrix [6,7]. At the early stage of aging, the H-phase nano-precipitates are coherent with the austenite matrix, yet, they lose some coherency with the martensite matrix due to the strain induced by matrix transformation and lattice mismatch [7]. Initially, H-phase precipitates nucleate as spherical particles and subsequently grow into spindle-shaped structures [24]. The precipitate size, volume fraction, and coherency can be tailored by varying the aging conditions [6–9,11,25–27].

* Corresponding author.
E-mail address: kelvin.xie@tamu.edu (K.Y. Xie).
[1] These authors contributed equally to this work.

https://doi.org/10.1016/j.actamat.2023.119642
Received 24 July 2023; Received in revised form 22 December 2023; Accepted 28 December 2023
Available online 29 December 2023

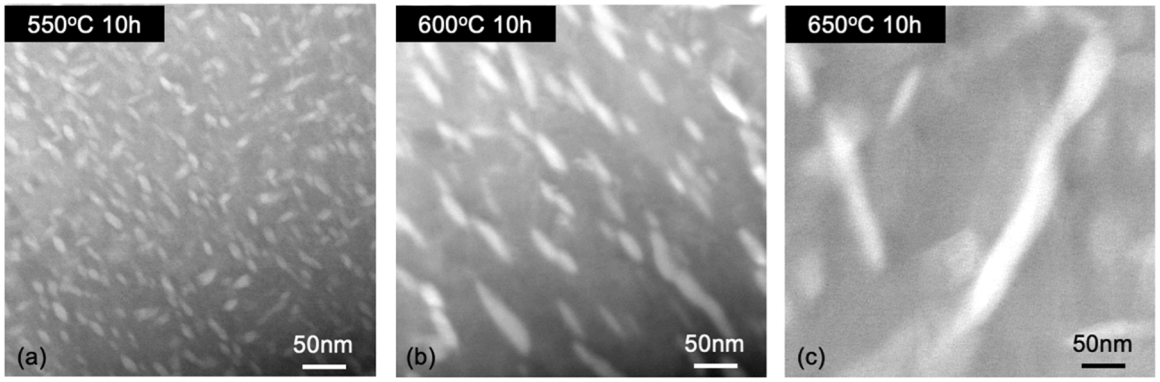

Fig. 1. HAADF-STEM images of $Ni_{50.3}Ti_{29.7}Hf_{20}$ aged at (a) 550 °C, (b) 600 °C, (c) 650 °C for 10 h.

The aging process and, consequently, the precipitation formation are known to influence the transformation behavior, including TTs, thermal hysteresis, and dimensional and thermal stability in NiTiHf high-temperature SMAs. In $Ni_{50.3}Ti_{29.7}Hf_{20}$, it has been observed that increasing the aging temperatures and times results in further growth of precipitates, ranging from nanometer to micron sizes. There is a general trend of increasing TTs for samples aged at higher temperatures or for longer times [11]. This is because H-phase precipitates are rich in Hf and Ni. As Ni content has a significantly greater effect on TTs than Hf content, the removal of Ni from the matrix increases the phase transformation temperature [28]. Furthermore, nanometer-sized precipitates have been reported to improve strength, dimensional stability, thermal stability, work output, superelasticity, and fatigue performance [8–12, 29]. On the contrary, coarse precipitates lead to poor thermomechanical properties in NiTiHf SMAs [9,11,30,31]

Despite significant advancements in the understanding of high-temperature NiTiHf SMAs, there are still several unanswered questions regarding their property-microstructure relationship. For instance, previous studies have indicated that (011) type I twins are predominant in certain NiTiHf SMAs with precipitates [7,11,12,32–38]. However, it is unclear whether the twinning microstructure is influenced by aging condition. Additionally, there is a need to explain how the observed changes in thermomechanical properties are linked to the microstructure. In this study, we used a nominal $Ni_{50.3}Ti_{27.9}Hf_{20}$ (at. %) SMA as the model system. To obtain nano-scale diffraction information and generate transmission electron microscopy (TEM)-based orientation maps, we employ precession electron diffraction (PED), which provides insights not easily obtained through conventional TEM methods. Subsequently, we utilize the newly acquired microstructural information to elucidate the thermomechanical properties observed through isobaric thermal cycling (ITC) and differential scanning calorimetry (DSC) tests.

2. Materials and methods

2.1. Material processing

A bulk sample of $Ni_{50.3}Ti_{29.7}Hf_{20}$ (at.%) SMA was synthesized by vacuum induction melting high purity (99.98 % Ni, 99.95 % Ti, and 99.9 % Hf) pellets. The material was then homogenized under vacuum at 1050 °C for 72 h, air cooled and subsequently hot forged to achieve an R ratio of 2.35:1. Test samples were prepared by wire electrical discharge machining (EDM) and were vacuum sealed in a quartz tube and back-filled with Ar. Samples were then subjected to a solution heat treatment (SHT) at 900 °C for 1 h, followed by water quenching. Three different aging treatments were performed on the solutionized samples to grow precipitates of different sizes. Aging was carried out at 550 °C, 600 °C, and 650 °C for 10 h followed by air cooling. Further analysis was conducted on samples in all four conditions: SHT, 550 °C-10 h, 600 °C-10 h, and 650 °C-10 h. It should be noted that precipitate size and number density can also be engineered by holding the aging temperature constant and varying the aging time or by varying both temperature and time [27].

2.2. Microstructural characterization

For TEM and PED analyses, specimens were mechanically polished to a nominal thickness of 100 μm using SiC paper ranging from 400 to 1200 grit. Polished specimens were punched into 3 mm diameter discs and electropolished using a *Tenupol-5* polishing system with a 30 % nitric acid in ethanol solution at −30 °C.

TEM images were captured using an *FEI TECNAI G2 F20 ST FE-TEM* equipped with a high-angle annular dark-field (HAADF) detector operating at 200 keV, with the images acquired near the perforations in the TEM specimens. To reveal the orientation relationship between martensite laths and the orientation of defects within the martensite laths, we employed PED. The *NanoMEGAS* PED system records electron diffraction pattern for each pixel, with a resolution as low as 3 nm. The experimentally acquired diffraction patterns are then compared with the simulated diffraction patterns in the database to determine the crystal structure and orientation of each pixel [39–41]. In this study, we acquired diffraction patterns with a step size of 20 nm and a precession angle of 0.3°. Before indexing the diffraction patterns, an automated contrast limited adaptive histogram equalization (CLAHE) algorithm [42] was applied to all diffraction patterns to enhance the diffraction signal while keeping the background low. Our previous work has demonstrated the diffraction pattern indexing quality dramatically improved after applying the auto-CLAHE algorithm [43]. The diffraction indexing was based on the B19′ martensite lattice parameters reported in previous studies by Evirgen et al. [44] and Benafan et al. [12]. When presenting the diffraction results in this work, the patterns were not rotated to offset the magnetic rotation of the instrument.

2.3. Thermo-mechanical characterization

A *TA Instruments Q2000* DSC was used to measure the stress-free phase transformation temperatures of both SHT and aged samples. The dimensions of the DSC samples were 5 mm × 5 mm × 1 mm. The DSC specimens were thermally cycled 3 times with a heating and cooling rate of 10 °C/min from -50 °C (SHT) or 0 °C (aged) to 300 °C in the calorimeter. Transformation temperatures were determined from the DSC data using the slope line extension method [30]. Full width at half maximum (FWHM) was used as a measure of the spread of temperatures over which the phase transformation occurs.

Isobaric thermal cycling (ITC) experiments were conducted using a servo-hydraulic *MTS* test frame on dog-bone-shaped miniature tension specimens with dimensions of 8 mm × 3 mm × 1.5 mm. ITC experiments were performed by applying a constant force to the sample and conducting one complete thermal cycle from an upper cycle temperature

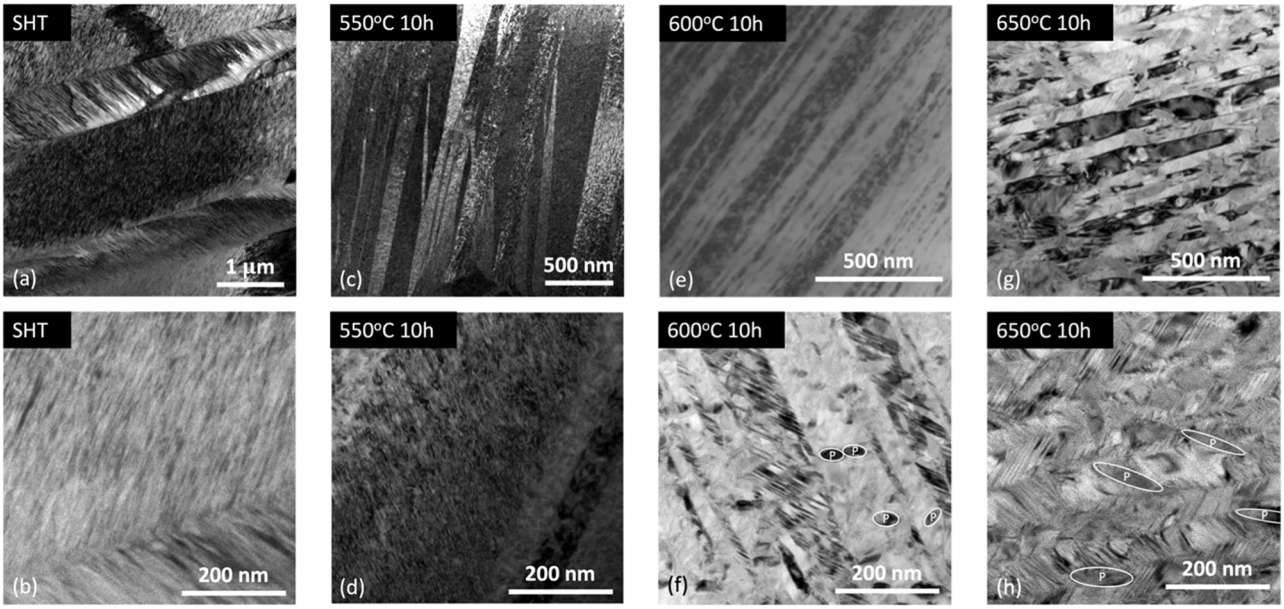

Fig. 2. Regular BF-TEM images of $Ni_{50.3}Ti_{29.7}Hf_{20}$ SMAs subjected to different heat treatments show each sample's martensite microstructure. (a) and (b) SHT, (c) and (d) aged at 550 °C, (e) and (f) 600 °C, (g) and (h) 650 °C for 10 h. (b), (d), (f), and (h) highlight the high-density inner twins in each sample with a higher magnification. Some precipitates in 600 °C and 650 °C-aged samples are highlighted with ellipses and the letter 'P'.

(UCT) to a lower cycle temperature (LCT) and back to the UCT. The load was then increased when the sample again reached the UCT and thermally cycled. This process was repeated for five stress levels (50, 100, 150, 200, 300 MPa). The LCT was 50 °C (for SHT sample) or 100 °C (for aged samples) and the UCT was 300 °C for all samples. The LCTs and UCTs were chosen to ensure full transformation under each applied stress level. Strain was measured during thermal cycling using an *MTS* high-temperature extensometer directly attached to the gage section of the samples. The actuation strains (ε_{act}) were calculated following ASTM E3097-23 [45], as the difference between the strains at the LCT and the UCT during the heating cycle (LCT à UCT). Samples were heated and cooled by conduction from the tension grips. The grips were heated with heating bands, and cooled by circulating liquid nitrogen through copper tubes wrapped around the grips. The rate of heating and cooling during isobaric thermal cycling tests was maintained at 10 ± 2 °C/min, and the temperature was measured using a K-type thermocouple that was directly attached to the gage section of the samples.

3. Results and discussions

3.1. Microstructural characterization

Aged $Ni_{50.3}Ti_{29.7}Hf_{20}$ SMAs exhibit precipitates of varying sizes and number densities, depending on the specific aging conditions, which are revealed through high-angle annular dark-field scanning transmission electron microscopy (HAADF-STEM) imaging, as shown in Fig. 1. The observed precipitates are rich in Hf and Ni compared to the matrix, thus appearing bright in the HAADF-STEM images. These precipitates were identified to be the H-phase precipitates, like those reported in [6,23,24]. The micrographs were captured at the same magnifications to enable direct comparison. At the aging temperature of 550 °C, high-density nano-precipitates of approximately 20.9 ± 3.3 nm in length were observed (Fig. 1a). Increasing the aging temperature to 600 °C results in the growth of larger precipitates, approximately 59.8 ± 14.5 nm in length, with a decreased number density (Fig. 1b). Further elevating the aging temperature to 650 °C leads to even larger precipitates, approximately 161.5 ± 39.9 nm in length, and an even lower number density (Fig. 1c). The distribution of precipitates in all aged samples was observed to be uniform [25]. The volume fractions of precipitates were measured in the previous study as 8.5 ± 0.3 %, 9.8 ± 3 %, and 12.9 ± 2.5 % in the 550 °C-aged, 600 °C-aged, and 650 °C-aged samples, respectively [25].

Regular bright-field (BF) TEM imaging was used to investigate the martensite microstructure in each sample (Fig. 2). The characteristic feature observed in all samples is the near-parallel twinned martensite plates, consistent with the literature [11,24]. However, the width of these martensite plates varies among the samples. In the SHT samples, the martensite plates exhibit the greatest width, ranging from 1 to 2 μm (Fig. 2a). With the introduction of precipitation through aging treatments, a significant reduction in martensite plate width is observed, ranging from 200 to 500 nm (Fig. 2c). When the aging temperature increases from 550 °C to 600 °C (while maintaining a constant aging time of 10 h), the width of the martensite plates further decreases to approximately 100 nm (Fig. 2e). However, further increasing the temperature to 650 °C did not further reduce the martensite plate width; it remains around 100 nm (Fig. 2g).

Another common feature among these samples is the presence of (001) compound twins, which were consistently observed within the martensite plates in all samples. (001) compound twins have also been reported as inner twins in other aged NiTiHf alloys [7,11,12,32–37]. In this study, the (011) compound twin densities in the SHT (Fig. 2b) and 550 °C-aged (Fig. 2d) samples are very high and difficult to directly measure from the BF-TEM images. Their densities were observed to decrease in the 600 °C-aged (Fig. 2e) and 650 °C-aged (Fig. 2f) samples, with the twin width in the range of 2.5–4 nm.

These microstructural characteristics, in particular the interface types revealed by PED, are listed in Table 2 for a direct comparison. Small precipitates with small interparticle spacing tend to be embedded in martensite grains, which limits the growth of the martensite plates. Hence, the 550 °C-aged sample exhibits thinner martensite plates compared to the SHT samples. However, when precipitates and their interparticle spacing are larger (e.g., in the 650 °C-aged samples), the further refined martensite plates are formed between these precipitates, and the width of martensite plates is governed by the interparticle spacing, and large precipitates act as a barrier against martensite plate growth [11,46]. Similarly, the inner twin width is also affected by the precipitate size as shown in Fig. 2. The twin size is very small in the SHT case, and the twin widths increase with the precipitate size. The twin

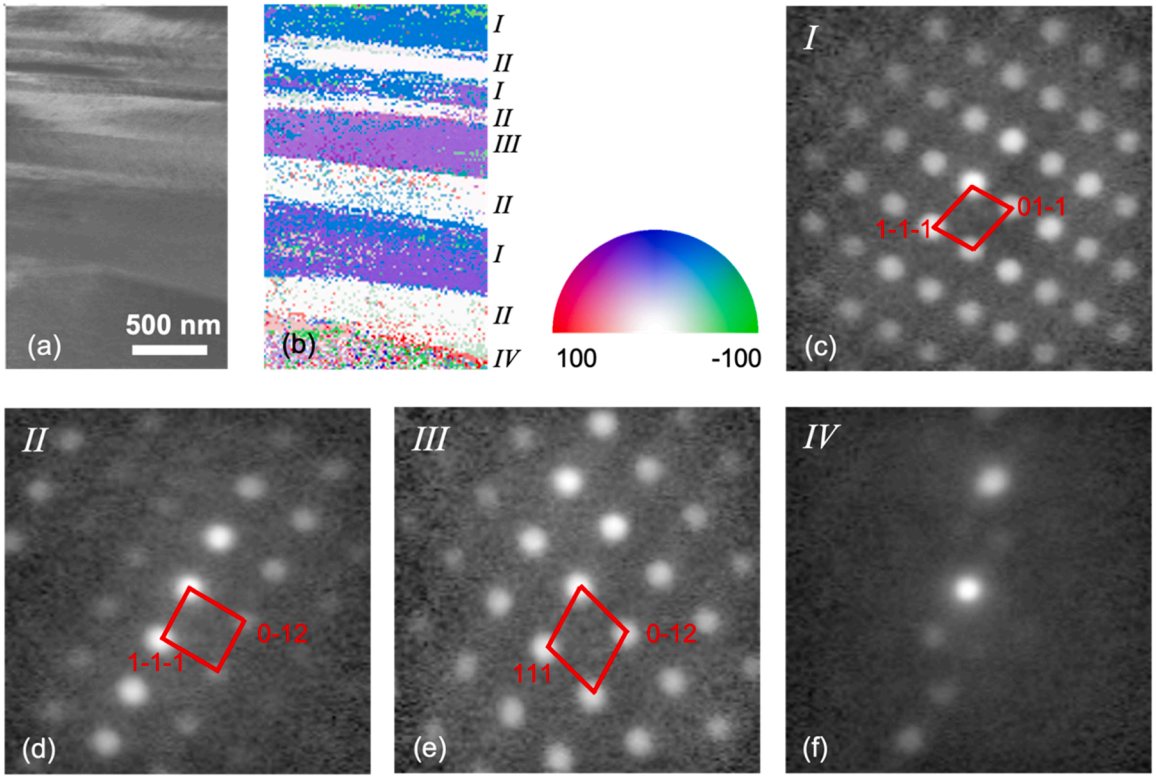

Fig. 3. (a) Virtual bright-field image of the SHT sample showing a number of martensite plates. (b) The corresponding orientation map. (c–g) Diffraction patterns from variant I–IV in the orientation map. Red parallelograms are used to demonstrate the symmetry of each diffraction pattern.

widths in the 600 °C and 650 °C samples are somewhat comparable. In other words, while the martensite plate interface density increases with the precipitate size, the inner twin interface density seems to drop. The density of these interfaces and their mobility is expected to influence the martensite transformation kinetics, actuation strain, and temperature (or stress) range of the transformation [47].

Next, we utilized PED to reveal the martensite variant numbers and orientation relationship between the martensite plates in the SHT and aged samples. Fig. 3a shows the virtual bright-field (VBF) image of the mapped region in the SHT $Ni_{50.3}Ti_{29.7}Hf_{20}$ sample. Fig. 3b shows the corresponding orientation map, which provides insights into the martensite variants present in the sample. Within the mapped region, nine martensite plates but only four martensite variants were observed. These variants were labeled as variant I (blue), variant II (white), variant III (purple), and variant IV (mixed colors). The colors were assigned based on the inverse pole figure color key. The diffraction patterns corresponding to each variant are shown in Fig. 3c–f. It is important to note that the low symmetry of the martensite crystals (monoclinic unit cell) resulted in a relatively poor indexing quality [48]. All subsequent orientation maps suffer from this limitation. Nevertheless, careful examination and analysis were conducted to confirm the martensite variant numbers. Additionally, it was observed that the arrangement of neighboring martensite variants followed certain patterns. For instance, variant II could be adjacent to either variant I or variant II, while variant I was not found to be adjacent to variant III. Moreover, no well-defined twin relationship between the martensite plates was identified. For instance, although the (1-1-1) planes in variant II were found to be parallel to the (111) planes in variant III, this is not a twin relationship. These observations are consistent with our previous study [49].

In contrast, the aged samples show very different martensite variant numbers and orientation relationships . Fig. 4 shows the maps from two regions in the 550 °C-aged samples. In the first region, the virtual dark-field (VDF) map (Fig. 4a) reveals the martensite plates of width tens to a few hundred nanometers. The corresponding orientation map (Fig. 4b) combined with careful inspection shows predominantly two variants: variant I (white) and variant II (blue). The diffraction patterns are shown in Fig. 4c and d, indicating both variants were tilted to the [100] zone axis. The two diffraction patterns are similar in shape but have slight differences. To highlight the differences between them, the diffraction spots of (020), (002), and (022) were labeled in both patterns. Both diffraction patterns share the (022) diffraction spots and exhibit a twin relationship (Fig. 4e), indicating the (011) type I twin relationship between variants I and II.

To demonstrate the reproducibility of the result above, more regions were mapped and one more example is shown in Fig. 4f–l. Fig. 4f shows the VDF image of the mapped region, revealing the martensite plates. The corresponding orientation map is shown in Fig. 4g, which is mainly composed of two variants: variant I (blue) and variant II (white). Fig. 4h and i show that both variants were tilted close to the [100] zone axis. The (011) and (010) diffraction spots were marked. The diffraction patterns share the (011) reflections while displaying a twin relationship, indicating the type I (011) twin (top schematic in Fig. 4l). In addition, two more variants, variant III (green) and variant IV (pink), were identified in the top right corner in the orientation map. The diffraction patterns (Fig. 4j and k) suggest the crystals were tilted to the [01–1] zone axis for both variants III and IV. The (100), (011), and (111) diffraction spots were also marked. Variants III and IV also exhibit a twin relationship and share the (011) diffraction spots, also indicating the type I (011) twin (bottom schematic in Fig. 4l).

Combining the aforementioned observations of the 550 °C-aged sample, two key findings emerge. First, a significant portion of the material exhibits a predominant presence of two martensite variants arranged in a pattern of •••I II I II•••, contrasting the four martensite variants observed in the SHT sample. Second, the martensite plates in the aged sample demonstrate a well-defined type I (011) twin orientation relationship, which also differs from the SHT sample.

We further conducted PED characterization on the 600 °C-aged sample to investigate the influence of increasing precipitate size on

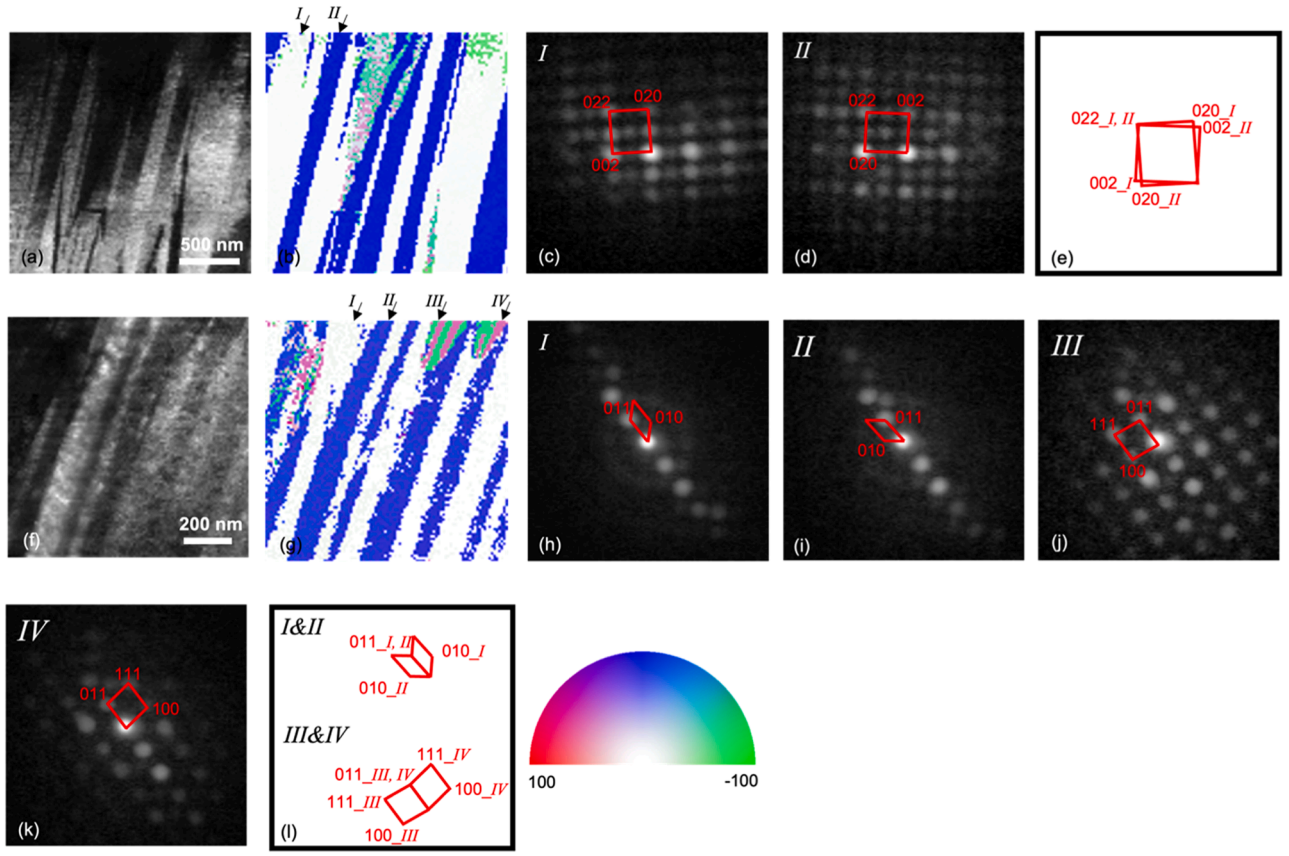

Fig. 4. (a) Virtual dark-field image of the 550 °C 10 h sample showing a number of martensite plates. (b) The corresponding orientation map. (c, d) Diffraction patterns from variant I and II in the orientation map. Red parallelograms are used to demonstrate the symmetry of each diffraction pattern. (e) Comparison between parallelograms from the diffraction pattern of each variant in the orientation map, showing the orientation relationship between them. (f–l) correspond to (a–e) but in a different area of the specimen to highlight the consistency and repeatability of the variant numbers and the orientation relationship between the martensite plates.

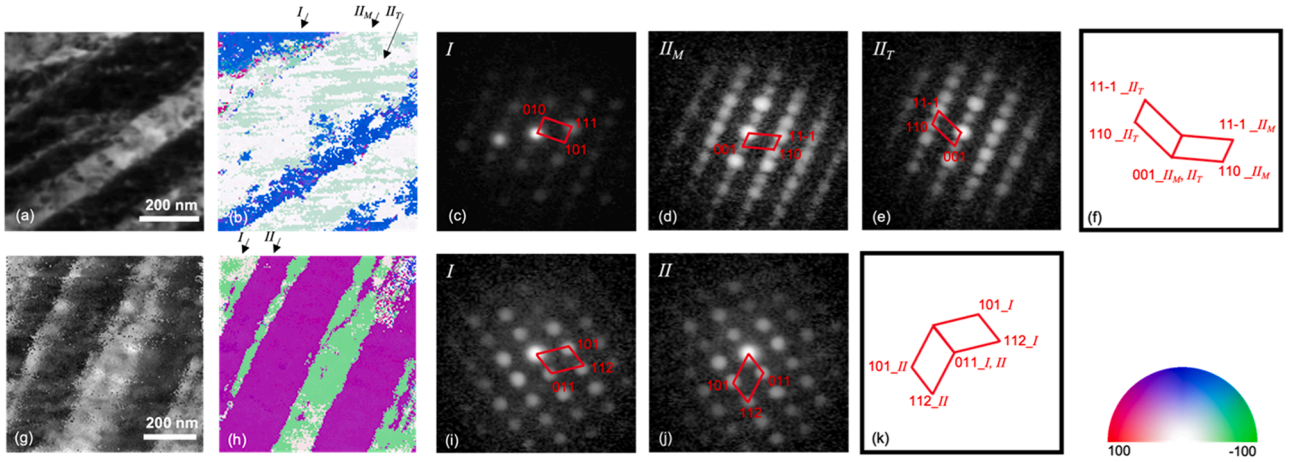

Fig. 5. (a) Virtual dark-field image of the 600 °C 10 h sample showing a number of martensite plates. (b) The corresponding orientation map. (c–e) Diffraction patterns from variant I, II_M and II_T in the orientation map. (f) Comparison between parallelograms from the diffraction pattern of variant II_M and II_T in the orientation map, showing the orientation relationship between them. Red parallelograms are used to demonstrate the symmetry of each diffraction pattern. (g–k) correspond to (a–f) but in a different area of the specimen to highlight the consistency and repeatability of the variant numbers and the orientation relationship between the martensite plates.

martensite characteristics. Fig. 5 shows two selected regions that were examined. In region one, the VDF image (Fig. 5a), orientation map (Fig. 5b), and diffraction analyses (Fig. 5c–e) uncover two martensite variants: variant I (blue) and variant II (green and white). Variants I and II were tilted to the [10–1] (Fig. 5c) and variant II [1–10] (Fig. 5d and e) zone axes, respectively. In this orientation, one cannot simply derive the orientation relationship between the martensite variants. We note variant II contains two types of diffraction patterns (Fig. 5d and e), both aligned along the [1–10] zone axis and sharing the (001) diffraction spots, suggesting the (001) compound twin relationship between them. Similar observations were made in region II, with the VDF (Fig. 5 g) showing martensite plates and the orientation map (Fig. 5h) and

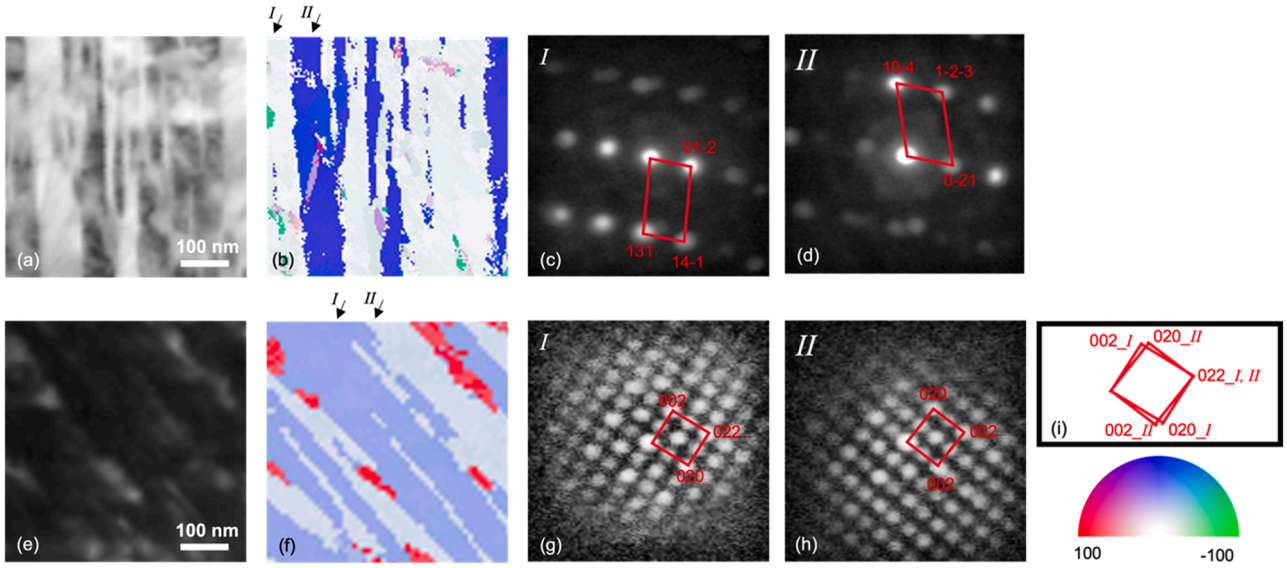

Fig. 6. (a) Virtual dark-field image of the 650 °C 10 h sample showing a number of martensite plates. (b) The corresponding orientation map. (c, d) Diffraction patterns for variant I and II in the orientation map. Red parallelograms are used to demonstrate the symmetry of each diffraction pattern. (e–h) correspond to (a–d) but in a different area of the specimen to highlight the consistency and repeatability of the variant numbers and the orientation relationship between the martensite plates. (i) Comparison between parallelograms from the diffraction pattern of each variant in the orientation map, showing the orientation relationship between them.

diffraction spot analyses (Fig. 5i–k) revealing the martensite variant numbers and orientation relationship. Both variants (variant I green and variant II purple) were tilted to the [11-] zone axis. Both diffraction patterns share the (011) diffraction spot, confirming the (011) type I twin relationship between the martensite variants. Thus, it can be concluded that, in the 600 °C-aged sample, the number of martensite variants and their orientation relationship remain consistent with those of the 550 °C sample.

The same microscopy approaches were used to analyze samples aged at 650 °C, with micrographs presented in Fig. 6. VDF images reveal the presence of martensite plates (Fig. 6a and e). PED analysis showed that there are predominantly two variants alternating in both regions, with variant I (white) and variant II (blue) in region one (Fig. 6b) and variant I (blue) and variant II (light grey-blue) in region two (Fig. 6f). For region one, the diffraction patterns (Fig. 6c and d) revealed that the variants are oriented along the [-721] and [812] zone axes. In this diffraction condition, the martensite plate interfaces are not parallel to the electron beam, hence their characteristic cannot be determined. In contrast, for region two, both martensite variants were tilted to the [100] zone axis (Fig. 6g and h). Notably, both diffraction patterns shared the (011) plane and exhibited twin symmetry, confirming the type I (011) twin relationships between the martensite plates in this sample.

The effect of aging on the martensitic variant characteristics in the $Ni_{50.3}Ti_{29.7}Hf_{20}$ sample is noteworthy. Fig. 3 and our previous work [49] demonstrate that the SHT sample exhibited four martensitic variants. However, as depicted in Figs. 4–6, the aged $Ni_{50.3}Ti_{29.7}Hf_{20}$ samples (displayed predominantly two martensitic variants. This reduction in number of variants was accompanied by a change in the orientation relationship between the variants. In the SHT $Ni_{50.3}Ti_{29.7}Hf_{20}$ sample, the observed orientation relationships included (1 1 0.64) Type II twin boundaries, junction planes that $(1\ 1\ 1)_{variant\_I}$ // $(1\ 1\ 0.64)_{variant\_II}$, as well as (111) type I twin boundaries [49]. In contrast, the aged samples exhibited a simplified orientation relationship characterized by (011) type I twin boundaries. Previous papers on aged NiTiHf alloys also reported the presence of (011) type I twins [11,12,50]. In this work, we mapped multiple areas and a large number of interfaces between martensite variants, and demonstrated the (011) type I twin boundary is the dominant twin boundary in precipitate-bearing $Ni_{50.3}Ti_{29.7}Hf_{20}$ SMAs.

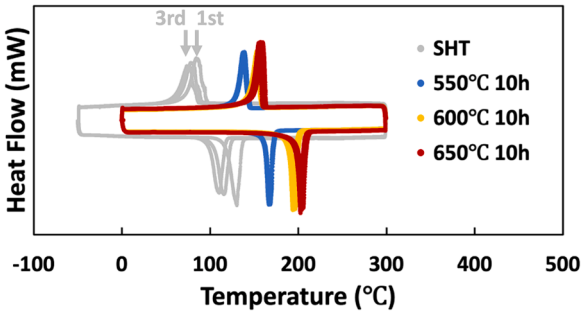

Fig. 7. DSC response of the $Ni_{50.3}Ti_{29.7}Hf_{20}$ alloy in the SHT and aged conditions.

The reduction in the number of martensite variants and the change in orientation relationship observed in the aged samples can be attributed to the presence of H-phase precipitates. In the SHT sample, martensite nucleation and growth have more flexibility, allowing for a greater number of martensite variants to accommodate the geometric constraints imposed by neighboring austenite grains. However, in samples with precipitates, the martensite plates tend to orient themselves in a way that minimizes the misfit strain between the martensite matrix and the non-transformable precipitates, resulting in a reduced number of martensite variants. Hence, the presence of precipitates imposes additional constraints, leading to a lower degree of freedom in the martensitic transformation process. This reduction in martensite variants also contributes to a decrease in the possible orientation relationships between the martensite plates. The prevalence of type I (011) twin in the aged samples is likely due to its higher coherency and lower energy compared to other types of interfaces observed in the SHT sample.

3.2. *Thermomechanical properties characterization*

To explore the impact of aging and precipitation on the thermomechanical properties of the samples, we employed DSC to examine the phase transformation behavior and ITC experiments to investigate the shape memory effect in the NiTiHf SMAs. A correlation between the

Table 1
Transformation temperatures and thermal hysteresis in the first heating cooling cycle, extracted from the DSC curves of $Ni_{50.3}Ti_{29.7}Hf_{20}$ HTSMAs which are solution heat treated (SHT) or aged at different conditions. Thermal stability is calculated based on the martensite start temperatures from the first cycle (M_{s1}) and from the third cycle (M_{s3}). M_s: Martensite start temperature; A_f: Austenite finish temperature.

Condition	Transformation temperature (°C)		Hysteresis (A_f–M_s) (°C)	Thermal stability (M_{s1}–M_{s3}) (°C)
	M_s	A_f		
SHT	88	142	54	10
550 °C 10h	147	180	33	1.7
600 °C 10h	160	201	41	3.4
650 °C 10h	162	208	46	4.4

Table 2
Microstructural characteristics of $Ni_{50.3}Ti_{29.7}Hf_{20}$ HTSMAs solution heat treated (SHT) and aged at different conditions.

Samples	SHT	550 °C 10 h	600 °C 10 h	650 °C 10 h
Martensite morphology	Parallel martensite plates			
Martensite thickness	1, 2 um	200–500 nm	~100 nm	~100 nm
Precipitate size (length)	–	20.9 ± 3.3nm	59.8 ± 14.5 nm	161.5 ± 39.9 nm
Precipitate volume fraction [25]	–	8.5 ± 0.3 %	9.8 ± 3 %	12.9 ± 2.5 %
Martensite variant numbers	4	2	2	2
Martensite plate interfaces	(1 1 0.64) type II, $(111)_{variant\_I}$ // $(1\ 1\ 0.64)_{variant\_II}$, (111) type I	(011) type I	(011) type I	(011) type I
Inner twin	(001) compound			

measured thermomechanical properties and the microstructure observed in the previous section is then established.

The DSC curves of SHT and aged samples are shown in Fig. 7. The first three heating-cooling cycles of each sample are shown. There are several salient differences between the SHT and aged samples. Firstly, the aging treatment significantly increased the TTs of $Ni_{50.3}Ti_{29.7}Hf_{20}$. Taking the DSC results of the first cycle for each sample as an example (Table 1), the martensitic transformation start temperature (M_s) of the SHT sample is 88 °C, then increases to 147 °C in the 550 °C-aged sample. The M_s further increases to 160 °C and 162 °C in the 600 °C-aged and 650 °C-aged samples, respectively. Similar trends are also present for the martensitic transformation finish temperature (M_f), austenitic transformation starting temperature (A_s), and austenitic finishing temperature (A_f). The increase in TTs is due to the removal of Ni from the matrix to form the H-phase precipitates. This observation is consistent with previous studies on the NiTiHf of the same composition but aged under different conditions [11], as well as in NiTiHf of similar compositions [9, 26] NiTiZr [51]. We also note that the TTs of the 600 °C-aged and 650 °C-aged samples are very similar. This is because the H-phase precipitates are of similar volume fractions, and the matrixes are of similar composition, as calculated in previous study [25].

Secondly, an apparent improvement in the thermal cycling stability of $Ni_{50.3}Ti_{29.7}Hf_{20}$ was achieved after aging. The thermal cycling stability is determined by the difference between the M_s values in the first and third thermal cycles ($M_{s3} - M_{s1}$) (Table 1). A larger difference indicates poorer thermal cycling stability. For the SHT sample, this value is 10 °C. After aging at 550 °C for 10 h, this difference sharply decreased to 1.7 °C. In the samples aged at 600 °C and 650 °C, this value was 3.4 °C and 4.4 °C, respectively. The drift of TTs after thermal cycling can be attributed to chemical short-range ordering formed at elevated temperatures during DSC and/or the generation of dislocations during the martensite-austenite transformation [47,52]. The dispersion of the precipitates used up chemical short-range ordering and hardens the aged samples and suppresses the dislocation propagation, which improves the thermal cycling stability.

Thirdly, we observed a notable change in the shape of the DSC peaks before and after aging. Initially, the DSC peak of the SHT sample exhibits a broader profile. Following aging at 550 °C, 600 °C, and 650 °C, the peak shape became much steeper. To quantify this change, we employed the full width at half maximum (FWHM) measurement as an indicator of peak shape, using the first cooling peak as an example to highlight the differences. The SHT sample displayed a wider peak with an FWHM of 12.2 °C. The aged samples exhibited sharper profiles, with FWHM values of 7.8 °C, 8.0 °C, and 7.4 °C for the ones aged at 550 °C, 600 °C, and 650 °C, respectively. A similar trend was also observed in the heating peaks and peaks in the second and third heating-cooling cycles.

The variations in the DSC peak shape before and after the aging of the $Ni_{50.3}Ti_{29.7}Hf_{20}$ samples can be attributed to microstructural changes. Although both the SHT and aged samples exhibited martensitic plates with the (001) compound twins, notable differences were observed in the number of martensite variants and their orientation relationship pre- and post-aging. The SHT sample displayed a higher number of martensitic variants and a more complex orientation relationship, leading to a wider temperature range for the nucleation and growth of each variant during the martensitic transformation. Consequently, the DSC cooling peak appeared broader. In contrast, the aged sample exhibited a reduced number of martensitic variants (two) and a uniform (011) type I twin orientation relationship. As a result, the DSC peaks of the aged sample appeared sharper compared to those of the SHT sample, with minimal differences in their shapes.

ITC experiments were carried out to investigate the shape memory effect of the SHT and aged samples. The highest stress level we adopted was 300 MPa. This is because all aged samples failed below 400 MPa [26]. The hysteresis loops in Fig. 8 show one representative strain response of each sample as a function of temperature under a variety of stress levels ranging from 50 MPa to 300 MPa. The red and blue curves correspond to heating and cooling cycles, respectively. A quick inspection of the figure can lead to two observations. First, the TTs in the load-biased condition of all the samples are consistent with the trends obtained from the load-free DSC experiments in Fig. 7. The SHT sample exhibits the lowest TTs. As aging temperature increases, the TTs continue increasing but plateau at 600 °C. Second, the SHT sample exhibits the lowest actuation strains in most cases, compared to the aged samples.

The evolution of actuation strain has been extracted from the ITC results from Fig. 8 for quantitative comparisons between different samples (Fig. 9). In all $Ni_{50.3}Ti_{29.7}Hf_{20}$ samples, the actuation strains increased with increased applied stress, which is commonly known in both NiTiZr and NiTiHf [19,26,53]. This is mainly because the amount of reoriented/detwinned martensite increases with increasing stress levels. Moreover, of all three aged conditions, the 600 °C-aged sample consistently exhibited the highest actuation strains, regardless of the applied stress; the 550 °C-aged sample displayed the lowest actuation strain. The low actuation strains in 550 °C-aged samples are due to the high-density compound twins (Fig. 2d) and the dispersion of nano-scale H-phase precipitates embedded in the martensite plates. These precipitates can hinder the detwinning of the compound twins, reducing the actuation strain. In contrast, in the 600 °C-aged and 650 °C-aged samples, the compound twin density is relatively lower (Fig. 2f and h) and the larger H-phase precipitates preferentially reside at the martensite plate interfaces, making the detwinning process easier, hence resulting

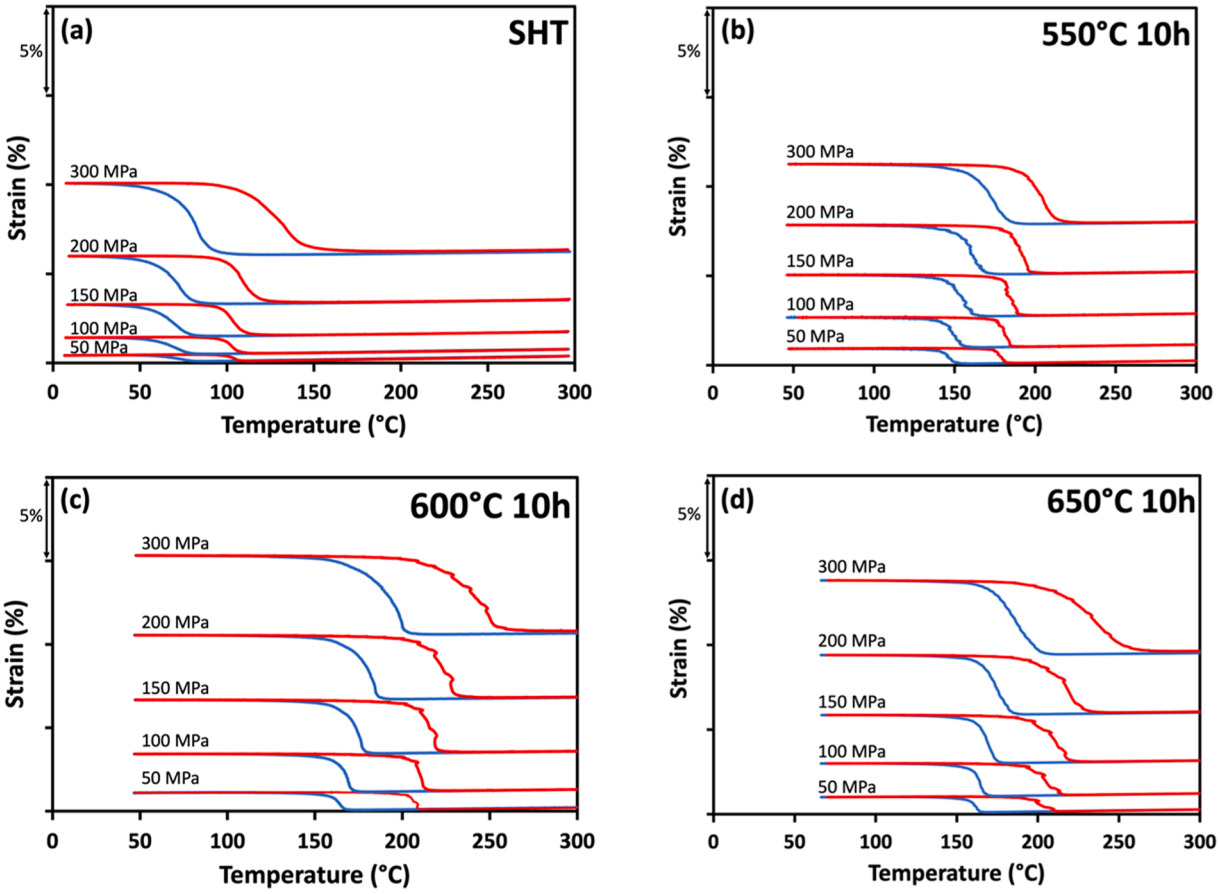

Fig. 8. Representative strain vs. temperature responses of $Ni_{50.3}Ti_{29.7}Hf_{20}$ HTSMA with different heat treatments in isobaric thermal cycling experiments under tension on the (a) SHT, (b) aged at 550 °C, (c) 600 °C, and (d) 650 °C for 10 h samples. The red curves indicate the heating cycles, and the blue curves indicate the cooling cycles.

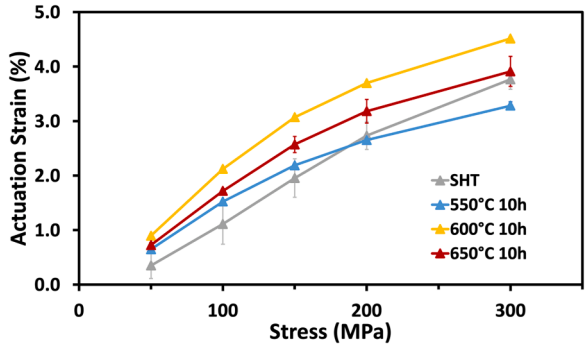

Fig. 9. The evolution of actuation strain as a function of applied stress, determined from the ITC results of $Ni_{50.3}Ti_{29.7}Hf_{20}$ HTSMA subjected to various heat treatments.

in larger actuation strains. Additionally, the actuation strain of the SHT sample is generally lower than all aged samples. This observation is similar to what Evirgen *et al.* reported in $Ni_{50.3}Ti_{34.7}Hf_{15}$ [26].

The increase in actuation strain in the aged $Ni_{50.3}Ti_{29.7}Hf_{20}$ samples is counterintuitive. One would expect the precipitate-bearing samples to have lower actuation strains due to a lower transformation volume as the H-phase precipitates are non-transformable. The retained or even improved actuation strain can be attributed to two factors: (1) the presence of precipitates and (2) the change in martensite characteristics. In the presence of precipitates, the materials become harder due to precipitate strengthening. Finer precipitates (corresponding to small interparticle distance) lead to harder materials. For example, the aged samples generally display higher transformation strains than the SHT counterpart. This is because, during thermal cycling, the combination of microplasticity and the elevated temperature can lead to dislocation generation in the SHT sample. These dislocations may impede phase transformation and result in a lower transformation strain. In contrast, in the aged samples, the precipitates are expected to hinder dislocation multiplication and glide, leading to higher actuation strains.

The improved transformation strains observed in the aged samples may also be explained by the martensite and twin characteristics. The SHT samples exhibit four martensite variants with complex orientation relationships: (1 1 0.64) type II twin $(1\ 1\ 1)_{variant\_I}$ // $(1\ 1\ 0.64)_{variant\_II}$, and (111) type I twin. Moreover, the SHT samples consists of much thinner inner twins than the aged samples. All the aged samples investigated in this study show predominantly two martensite variants with the well-defined (011) Type I twin orientation relationship. One should note that the changes in the number of the martensite variants and interface type are likely a result of minimizing elastic strain energy [54, 55] in the presence of precipitates. It is also interesting to point out that the two martensite variants and (011) Type I twins are consistent among all aged samples investigated in this study, indicating it is a general observation. Hence, they should be predominant microstructural features in many other precipitate-bearing NiTiHf SMAs. We infer the prevalence of (011) Type I twin contribute to the increased transformation strain in the aged samples due to its ease of reorientation compared to those observed in the SHT sample [56–58]. Nonetheless, the direct experimental measurement of the energy required to reorient for specific type of twin boundary or the mobility of the twin boundaries in SMAs is challenging. It can be a critical area of study for

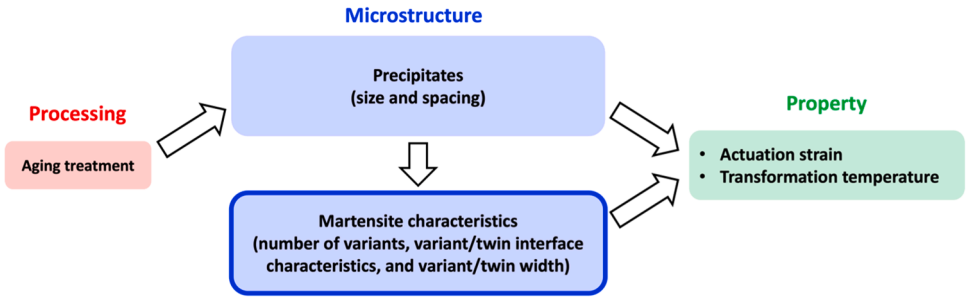

Fig. 10. The schematic highlighting the role of martensite variant number and boundary type in the processing-microstructure-property relationship of the $Ni_{50.3}Ti_{29.7}Hf_{20}$ HTSMA.

computational materials scientists.

4. Conclusions

In this work, we characterized and correlated the microstructure and thermomechanical properties of SHT and aged $Ni_{50.3}Ti_{29.7}Hf_{20}$ high-temperature SMAs (illustrated in Fig. 10), emphasizing the effects of precipitates and martensite variant characteristics. Aging resulted in the formation and growth of precipitates, and precipitates affected the martensite microstructure. The combined effect of precipitates and martensite microstructure led to changes in the transformation behavior of $Ni_{50.3}Ti_{29.7}Hf_{20}$ high-temperature SMAs. The more detailed findings and conclusions are summarized as follows:

- The samples remain martensitic after aging. There is a general reduction of martensite plate width in the aged samples, which is likely caused by the hindering effect of H-phase precipitates.
- Aging has a significant impact on the number of martensite variants and their orientation relationships. The SHT sample exhibits four martensite variants, whereas the aged samples show predominantly two variants when mapping similar numbers of martensite plates. Additionally, in the SHT sample, the martensite plates are separated by the (1 1 0.64) type II twin boundaries, junction planes that (1 1 1) variant_I // (1 1 0.64)variant_II, and (111) type I twin boundaries [49]. All aged samples, regardless of the precipitate size investigated in this study, contain the (011) type I twin boundaries. This difference may be explained by the strain compatibility requirement to accommodate the presence of the non-transformable during phase transformation.
- The aged samples demonstrate different, and in many cases improved, thermomechanical performance compared to the SHT sample, with further increased TTs, improved thermal cycling stability, narrower transformation temperature window, and improved actuation strain.
- For the aged samples, the increase in TTs is attributed to the decreased Ni content due to H-phase precipitation. The improved thermal stability can be explained by the hardening effect of the dispersion of precipitates. The narrower transformation temperature is likely caused by the reduced martensite variant and simplification of the martensite plate orientation relationship. The improved actuation strain is attributed to (1) the presence of precipitates and (2) the reduced martensite variant numbers and prevalent (011) type I twin boundary.

Overall, these findings shed light on the structure-property relationship of high-temperature SMAs using $Ni_{50.3}Ti_{29.7}Hf_{20}$ as the model system, highlighting the influence of aging and the role of H-phase precipitates in shaping the microstructure and thermomechanical properties.

Declaration of competing interest

The authors declare that they have no known competing financial interests or personal relationships that could have appeared to influence the work reported in this paper.

Acknowledgment

The authors would like to acknowledge the funding support from the National Science Foundation (NSF-DMR, Grant No.: 2004752, program managers: Dr. Judith Yang and Jonathan Madison) for the financial support for this research. The authors also would like to acknowledge the instrument and technical support from the Microscopy and Imaging Center at Texas A&M University.

References

[1] D. Tarniță, D. Tarniță, N. Bîzdoacă, I. Mîndrilă, M. Vasilescu, Properties and medical applications of shape memory alloys, Rom. J. Morphol. Embryol. 50 (1) (2009) 15–21.
[2] A. Riccio, A. Sellitto, S. Ameduri, A. Concilio, M. Arena, Shape memory alloys (SMA) for automotive applications and challenges, in: Shape Memory Alloy Engineering: For Aerospace, Structural and Biomedical, Butterworth-Heinemann, 2021, pp. 785–808.
[3] G. Firstov, J. Van Humbeeck, Y.N. Koval, High temperature shape memory alloys problems and prospects, J. Intell. Mater. Syst. Struct. 17 (12) (2006) 1041–1047.
[4] J. Ma, I. Karaman, R.D. Noebe, High temperature shape memory alloys, Int. Mater. Rev. 55 (5) (2010) 257–315.
[5] J. Van Humbeeck, High temperature shape memory alloys, J. Eng. Mater. Technol. 121 (1) (1999) 98–101.
[6] F. Yang, D. Coughlin, P.J. Phillips, L. Yang, A. Devaraj, L. Kovarik, R.D. Noebe, M. Mills, Structure analysis of a precipitate phase in an Ni-rich high-temperature NiTiHf shape memory alloy, Acta Mater. 61 (9) (2013) 3335–3346.
[7] R. Santamarta, R. Arróyave, J. Pons, A. Evirgen, I. Karaman, H. Karaca, R. Noebe, TEM study of structural and microstructural characteristics of a precipitate phase in Ni-rich Ni–Ti–Hf and Ni–Ti–Zr shape memory alloys, Acta Mater. 61 (16) (2013) 6191–6206.
[8] G. Bigelow, A. Garg, S. Padula Ii, D. Gaydosh, R. Noebe, Load-biased shape-memory and superelastic properties of a precipitation strengthened high-temperature $Ni_{50.3}Ti_{29.7}Hf_{20}$ alloy, Scr. Mater. 64 (8) (2011) 725–728.
[9] A. Evirgen, F. Basner, I. Karaman, R.D. Noebe, J. Pons, R. Santamarta, Effect of aging on the martensitic transformation characteristics of a Ni-rich NiTiHf high temperature shape memory alloy, Funct. Mater. Lett. 5 (04) (2012), 1250038.
[10] O. Benafan, R. Noebe, S. Padula, R. Vaidyanathan, Microstructural response during isothermal and isobaric loading of a precipitation-strengthened Ni-29.7 Ti-20Hf high-temperature shape memory alloy, Metall. Mater. Trans. A 43 (12) (2012) 4539–4552.
[11] H. Karaca, S. Saghaian, G. Ded, H. Tobe, B. Basaran, H. Maier, R. Noebe, Y. Chumlyakov, Effects of nanoprecipitation on the shape memory and material properties of an Ni-rich NiTiHf high temperature shape memory alloy, Acta Mater. 61 (19) (2013) 7422–7431.
[12] O. Benafan, A. Garg, R. Noebe, G. Bigelow, S. Padula Ii, D. Gaydosh, N. Schell, J. Mabe, R. Vaidyanathan, Mechanical and functional behavior of a Ni-rich $Ni_{50.3}Ti_{29.7}Hf_{20}$ high temperature shape memory alloy, Intermetallics 50 (2014) 94–107.
[13] M. Nishida, C. Wayman, A. Chiba, Electron microscopy studies of the martensitic transformation in an aged Ti-51at% Ni shape memory alloy, Metallography 21 (3) (1988) 275–291.
[14] A. Saigal, M. Fonte, Solid, shape recovered "bulk" Nitinol: part I—Tension–compression asymmetry, Mater. Sci. Eng. A 528 (16–17) (2011) 5536–5550.

[15] C.M. Laursen, N.J. Peter, G. Gerstein, H.J. Maier, G. Dehm, C.P. Frick, Influence of Ti_3Ni_4 precipitates on the indentation-induced two-way shape-memory effect in Nickel-Titanium, Mater. Sci. Eng. A 792 (2020), 139373.

[16] I. Kaya, H. Karaca, M. Nagasako, R. Kainuma, Effects of aging temperature and aging time on the mechanism of martensitic transformation in nickel-rich NiTi shape memory alloys, Mater. Charact. 159 (2020), 110034.

[17] T. Yu, Y. Gao, L. Casalena, P. Anderson, M. Mills, Y. Wang, H-phase precipitation and its effects on martensitic transformation in NiTi-Hf high-temperature shape memory alloys, Acta Mater. 208 (2021), 116651.

[18] A. Evirgen, J. Pons, I. Karaman, R. Santamarta, R. Noebe, H-Phase precipitation and martensitic transformation in Ni-rich Ni–Ti–Hf and Ni–Ti-Zr high-temperature shape memory alloys, Shape Mem. Superelast. 4 (2018) 85–92.

[19] H. Sehitoglu, L. Patriarca, Y. Wu, Shape memory strains and temperatures in the extreme, Curr. Opin. Solid State Mater. Sci. 21 (2) (2017) 113–120.

[20] M. Carl, J. Smith, R.W. Wheeler, Y. Ren, B. Van Doren, M.L. Young, High-energy synchrotron radiation X-ray diffraction measurements during *in situ* aging of a NiTi-15 at.% Hf high temperature shape memory alloy, Materialia 5 (2019), 100220.

[21] A. Young, R. Wheeler, N. Ley, O. Benafan, M. Young, Microstructural and thermomechanical comparison of Ni-rich and Ni-lean NiTi-20 at.% Hf high temperature shape memory alloy wires, Shape Mem. Superelast. 5 (2019) 397–406.

[22] M. Nematollahi, G.P. Toker, K. Safaei, A. Hinojos, S.E. Saghaian, O. Benafan, M. J. Mills, H. Karaca, M. Elahinia, Laser powder bed fusion of NiTiHf high-temperature shape memory alloy: effect of process parameters on the thermomechanical behavior, Metals 10 (11) (2020) 1522.

[23] X. Han, R. Wang, Z. Zhang, D. Yang, A new precipitate phase in a TiNiHf high temperature shape memory alloy, Acta Mater. 46 (1) (1998) 273–281.

[24] D. Coughlin, P. Phillips, G. Bigelow, A. Garg, R. Noebe, M. Mills, Characterization of the microstructure and mechanical properties of a 50.3 Ni–29.7 Ti–20Hf shape memory alloy, Scr. Mater. 67 (1) (2012) 112–115.

[25] J.K. Joy, T. Umale, D. Zhao, A. Solomou, K. Xie, I. Karaman, D.C. Lagoudas, Effects of microstructure and composition on constitutive response of high temperature shape memory alloys: micromechanical modeling using 3-D reconstructions with experimental validation, Acta Mater. 232 (2022), 117929.

[26] A. Evirgen, I. Karaman, R. Santamarta, J. Pons, R. Noebe, Microstructural characterization and shape memory characteristics of the $Ni_{50.3}Ti_{34.7}Hf_{15}$ shape memory alloy, Acta Mater. 83 (2015) 48–60.

[27] A. Shuitcev, Y. Ren, B. Sun, G. Markova, L. Li, Y. Tong, Y. Zheng, Precipitation and coarsening kinetics of H-phase in NiTiHf high temperature shape memory alloy, J. Mater. Sci. Technol. 114 (2022) 90–101.

[28] T. Umale, D. Salas, B. Tomes, R. Arroyave, I. Karaman, The effects of wide range of compositional changes on the martensitic transformation characteristics of NiTiHf shape memory alloys, Scr. Mater. 161 (2019) 78–83.

[29] S.M. Saghaian, H. Karaca, H. Tobe, M. Souri, R. Noebe, Y. Chumlyakov, Effects of aging on the shape memory behavior of Ni-rich $Ni_{50.3}Ti_{29.7}Hf_{20}$ single crystals, Acta Mater. 87 (2015) 128–141.

[30] A. Demblon, O. Karakoc, J. Sam, D. Zhao, K. Atli, J. Mabe, I. Karaman, Compositional and microstructural sensitivity of the actuation fatigue response in NiTiHf high temperature shape memory alloys, Mater. Sci. Eng. A 838 (2022), 142786.

[31] O. Karakoc, C. Hayrettin, A. Evirgen, R. Santamarta, D. Canadinc, R. Wheeler, S. Wang, D. Lagoudas, I. Karaman, Role of microstructure on the actuation fatigue performance of Ni-Rich NiTiHf high temperature shape memory alloys, Acta Mater. 175 (2019) 107–120.

[32] H. Sehitoglu, Y. Wu, L. Patriarca, G. Li, A. Ojha, S. Zhang, Y. Chumlyakov, M. Nishida, Superelasticity and shape memory behavior of NiTiHf alloys, Shape Mem. Superelast. 3 (2) (2017) 168–187.

[33] X. Han, W. Zou, R. Wang, Z. Zhang, D. Yang, Structure and substructure of martensite in a $Ti_{36.5}Ni_{48.5}Hf_{15}$ high temperature shape memory alloy, Acta Mater. 44 (9) (1996) 3711–3721.

[34] H. XD, C. CY, R. Wang, Z. Zhang, Y. DZ, Martensitic transformation in $Ti_{36.5}Ni_{48.5}Hf_{15}$ high temperature shape memory alloy, Mater. Trans. 38 (10) (1997) 842–851. JIM.

[35] Y. Zheng, L. Zhao, H. Ye, HREM study on the intervariant structure of Ti-Ni-Hf B19′ martensite, Scr. Mater. 38 (8) (1998) 1249–1253.

[36] Q. Wei, X. Han, Z. Zhang, The substructures of martensite in a $TiNiHf_{10}$ high temperature shape memory alloy, Mater. Lett. 60 (25–26) (2006) 3054–3058.

[37] A.P. Stebner, G.S. Bigelow, J. Yang, D.P. Shukla, S.M. Saghaian, R. Rogers, A. Garg, H.E. Karaca, Y. Chumlyakov, K. Bhattacharya, Transformation strains and temperatures of a nickel–titanium–hafnium high temperature shape memory alloy, Acta Mater. 76 (2014) 40–53.

[38] A. Shuitcev, D. Gunderov, B. Sun, L. Li, R. Valiev, Y. Tong, Nanostructured $Ti_{29.7}Ni_{50.3}Hf_{20}$ high temperature shape memory alloy processed by high-pressure torsion, J. Mater. Sci. Technol. 52 (2020) 218–225.

[39] E. Rauch, M. Véron, Automated crystal orientation and phase mapping in TEM, Mater. Charact. 98 (2014) 1–9.

[40] E.F. Rauch, J. Portillo, S. Nicolopoulos, D. Bultreys, S. Rouvimov, P. Moeck, Automated nanocrystal orientation and phase mapping in the transmission electron microscope on the basis of precession electron diffraction, Z. Kristallogr. 225 (2–3) (2010) 103–109.

[41] P.F. Rottmann, K.J. Hemker, Experimental observations of twin formation during thermal annealing of nanocrystalline copper films using orientation mapping, Scr. Mater. 141 (2017) 76–79.

[42] A.M. Reza, Realization of the contrast limited adaptive histogram equalization (CLAHE) for real-time image enhancement, J. VLSI Signal Process. Syst. Signal Image Video Technol. 38 (2004) 35–44.

[43] A.L. Wang, M.H. Hansen, Y.C. Lai, J. Dong, K.Y. Xie, Improving orientation mapping by enhancing the diffraction signal using Auto-CLAHE in precession electron diffraction data, Microstructures 3 (4) (2023), 2023036.

[44] A. Evirgen, I. Karaman, R. Santamarta, J. Pons, C. Hayrettin, R. Noebe, Relationship between crystallographic compatibility and thermal hysteresis in Ni-rich NiTiHf and NiTiZr high temperature shape memory alloys, Acta Mater. 121 (2016) 374–383.

[45] ASTM, Standard test method for uniaxial constant force thermal cycling of shape memory alloys, ASTM International, West Conshohocken, PA, 2023, p. 6.

[46] H. Karaca, E. Acar, G. Ded, B. Basaran, H. Tobe, R. Noebe, G. Bigelow, Y. Chumlyakov, Shape memory behavior of high strength NiTiHfPd polycrystalline alloys, Acta Mater. 61 (13) (2013) 5036–5049.

[47] R.F. Hamilton, H. Sehitoglu, Y. Chumlyakov, H. Maier, Stress dependence of the hysteresis in single crystal NiTi alloys, Acta Mater. 52 (11) (2004) 3383–3402.

[48] M.H. Hansen, A.L. Wang, J. Dong, Y. Zhang, T. Umale, S. Banerjee, P. Shamberger, M. Pharr, I. Karaman, K.Y. Xie, Crystallographic variant mapping using precession electron diffraction data, Microstructures 3 (2023), 2023029.

[49] J. Dong, T. Umale, B. Young, I. Karaman, K.Y. Xie, Structure and substructure characterization of solution-treated Ni50. 3Ti29. 7Hf20 high-temperature shape memory alloy, Scr. Mater. 219 (2022), 114888.

[50] A. Stebner, S. Vogel, R. Noebe, T. Sisneros, B. Clausen, D. Brown, A. Garg, L. Brinson, Micromechanical quantification of elastic, twinning, and slip strain partitioning exhibited by polycrystalline, monoclinic nickel–titanium during large uniaxial deformations measured via *in-situ* neutron diffraction, J. Mech. Phys. Solids 61 (11) (2013) 2302–2330.

[51] S.M. Kornegay, M. Kapoor, B.C. Hornbuckle, D. Tweddle, M.L. Weaver, O. Benafan, G.S. Bigelow, R.D. Noebe, G.B. Thompson, Influence of H-phase precipitation on the microstructure and functional and mechanical properties in a Ni-rich NiTiZr shape memory alloy, Mater. Sci. Eng. A 801 (2021), 140401.

[52] T. Simon, A. Kröger, C. Somsen, A. Dlouhy, G. Eggeler, On the multiplication of dislocations during martensitic transformations in NiTi shape memory alloys, Acta Mater. 58 (5) (2010) 1850–1860.

[53] O. Karakoc, K. Atli, O. Benafan, R. Noebe, I. Karaman, Actuation fatigue performance of NiTiZr and comparison to NiTiHf high temperature shape memory alloys, Mater. Sci. Eng. A 829 (2022), 142154.

[54] B. Ye, B. Majumdar, I. Dutta, Texture development and strain hysteresis in a NiTi shape-memory alloy during thermal cycling under load, Acta Mater. 57 (8) (2009) 2403–2417.

[55] J. Xiao, C. Cayron, M. Van der Meer, R. Logé, EBSD study of variant reorientation, texture, and twin formation in a martensitic NiTi alloy deformed in compression, Acta Mater. 264 (2023), 119553.

[56] F. Dalle, E. Perrin, P. Vermaut, M. Masse, R. Portier, Interface mobility in $Ni_{49.8}Ti_{42.2}Hf_8$ shape memory alloy, Acta Mater. 50 (14) (2002) 3557–3565.

[57] A. Shuitcev, L. Li, G. Markova, I. Golovin, Y. Tong, Internal friction in $Ti_{29.7}Ni_{50.3}Hf_{20}$ alloy with high temperature shape memory effect, Mater. Lett. 262 (2020), 127025.

[58] D. Shilo, E. Faran, B. Karki, P. Müllner, Twin boundary structure and mobility, Acta Mater. 220 (2021), 117316.